Universal Scaling Law for Jets of Collapsing Bubbles

D. Obreschkow, M. Tinguely, N. Dorsaz, P. Kobel, A. de Bosset, and M. Farhat

Phys. Rev. Lett. **107**, 204501 — Published 7 November 2011

DOI: 10.1103/PhysRevLett.107.204501

A Universal Scaling Law for Jets of Collapsing Bubbles

D. Obreschkow[1], M. Tinguely[1], N. Dorsaz[2], P. Kobel[3], A. de Bosset[1], and M. Farhat[1]
[1] *EPFL, Laboratoire des Machines Hydrauliques, 1007 Lausanne, Switzerland*
[2] *Department of Chemistry, University of Cambridge, Cambridge CB2 1EW, UK*
[3] *Max-Planck-Institut für Sonnensystemforschung, 37191 Katlenburg-Lindau, Germany*

Cavitation bubbles collapsing and rebounding in a pressure gradient $\boldsymbol{\nabla} p$ form a "micro-jet" enveloped by a "vapor jet". This letter presents unprecedented observations of the vapor jets formed in a uniform gravity-induced $\boldsymbol{\nabla} p$, modulated aboard parabolic flights. The data uncovers that the normalized jet volume is independent of the liquid density and viscosity and proportional to $\zeta \equiv |\boldsymbol{\nabla} p| R_0/\Delta p$, where R_0 the maximal bubble radius and Δp is the driving pressure. A derivation inspired by "Kelvin-Blake" considerations confirms this law and reveals its negligible dependence of surface tension. We further conjecture that the jet only pierces the bubble boundary if $\zeta \gtrsim 4 \cdot 10^{-4}$.

PACS numbers: 47.55.dp,47.55.dd,43.25.Yw

Jets produced by cavitation bubbles play a key role in cutting-edge technologies [1–3] and erosion [4–6]. These jets typically arise when a bubble collapses in a liquid of anisotropic pressure: At the ending collapse stage, the bubble surface develops a fast ($\gtrsim 100\,\mathrm{m\,s^{-1}}$ [4, 7, 8]) liquid jet. This "micro-jet" is directed inwards against the local pressure gradient $\boldsymbol{\nabla} p$ [9], defined in the absence of the bubble. While the bubble bounces off its enclosed gas, the micro-jet pierces the bubble and starts penetrating the liquid [4–6, 10] unless hitting a boundary. During the regrowth ("rebound", see Fig. 1a) of the bubble, the micro-jet becomes visible because of its conical shell of vapor [5, 11–13], here called the "vapor jet" (Fig. 3). The velocity and structure of jets of bubbles were modeled and measured in various cases [4, 8, 9, 14], but no general relation is known between the 'jet size' and the underlying pressure gradient. Such a relation would allow the modulation of jets by specifically engineering the pressure field; and, vise versa, permit a measurement of a pressure field via static images of jetting bubbles (Fig. 1).

This letter expands the state-of-the-art in three ways: (i) It presents the first high-speed movies of the jets caused by a gravity-induced pressure gradient $\boldsymbol{\nabla} p = \rho \boldsymbol{g}$ in normal gravity ($g = 9.81\,\mathrm{m\,s^{-2}}$, liquid density $\rho \approx 10^3\,\mathrm{kg\,m^{-3}}$). (ii) It performs a systematic study of the vapor jets observed while varying the maximal bubble radius, the liquid viscosity, the liquid pressure, and the pressure gradient. The latter is varied through a modulation of g aboard parabolic flights [25]. (iii) A statistical analysis of the data, backed-up by a theoretical derivation, reveals that the jet size scales with a dimensionless jet-parameter ζ.

Our experiment relies on a gravity-induced $\boldsymbol{\nabla} p$, which exhibits the unique advantage of being uniform in space and time. Such a gradient approximates, to first order, any smooth field $p(\boldsymbol{x}) = p(0) + \boldsymbol{x}^\dagger \boldsymbol{\nabla} p + \mathcal{O}(\partial^2 p)$, where $\boldsymbol{\nabla} p \equiv \boldsymbol{\nabla} p(0)$. Examples of $\boldsymbol{\nabla} p$ are

$$\boldsymbol{\nabla} p = \begin{cases} \rho \boldsymbol{g} & \text{gravitational field,} \quad (1a) \\ -\rho(\boldsymbol{v}\cdot\boldsymbol{\nabla})\boldsymbol{v} & \text{stat. potential flow,} \quad (1b) \\ +0.2 R_0 \Delta p\, \boldsymbol{h}/h^3 & \text{rigid flat surface,} \quad (1c) \\ -0.2 R_0 \Delta p\, \boldsymbol{h}/h^3 & \text{free flat surface,} \quad (1d) \end{cases}$$

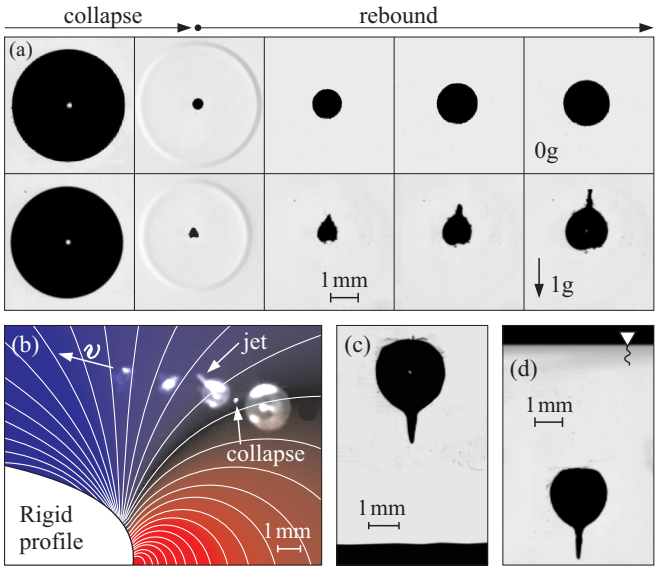

FIG. 1: Observations of the vapor jets directed against $\boldsymbol{\nabla} p$ during the rebound of cavitation bubbles. (a–d) match the cases of Eqs. (1a–d): (a) [video on-line] Collapse and rebound of a bubble ($R_0 \approx 4\,\mathrm{mm}$, $\Delta p \approx 15\,\mathrm{kPa}$) in '0g' (upper) and '1g' (lower); note the shock at the collapse. (b) Rebounding bubble ($R_0 \approx 1\,\mathrm{mm}$, $\Delta p \approx 100\,\mathrm{kPa}$) moving leftwards while jetting against the dynamic $\boldsymbol{\nabla} p$, orthogonal to the calculated p-contours. (c, d) Bubbles ($R_0 \approx 2\,\mathrm{mm}$, $\Delta p \approx 100\,\mathrm{kPa}$) rebounding with a jet *towards* a flat rigid surface ($h = 5.3 R_0$) and *away* from a flat free surface ($h = 5.1 R_0$), respectively. Images were taken using the setup of this letter (a,c,d) and a cavitation tunnel [15] (b).

where $\boldsymbol{v}$ is the velocity field, R_0 is the maximal bubble radius before collapse, $\boldsymbol{h}$ is the shortest vector from the surface to the bubble center, and $\Delta p \equiv p_0 - p_\mathrm{v}$ with p_0 being the pressure at cavity level and p_v the vapor pressure. Eq. (1b) follows from momentum conservation of an incompressible, stationary potential flow. Eqs. (1c, 1d) provide 'effective' time-averages of the self-generated pressure anisotropy of a bubble growing and collapsing close to a flat boundary: $\boldsymbol{\nabla} p$ is defined such that adding

a constant counter-gradient $-\nabla p$ would suppress the jet according to Ref. [16]. Jets described by Eqs. (1a–d) are shown in Fig. 1.

Experimental setup – Our setup (Fig. 2) uses a high-speed camera (Photron SA1.1) operating at up to 250,000 fps with exposure times of 370 ns to record a cavitation bubble generated by a pulsed laser (Quantel CFR 400, 532 nm, 8 ns). The laser is focussed inside a liquid volume to form a point-plasma [17] (diameter $\lesssim 0.1$ mm), which quickly cools and condensates while growing a bubble that subsequently collapses and rebounds. Whereas past studies [5, 6, 18] used lenses to focus a laser, we here use for the first time a concave parabolic mirror (Fig. 2). We found the mirror technique to produce bubbles of much higher sphericity, since reflection is independent of the liquid's refractive index and mirrors allow large angles of convergence (here 53°) without spherical aberration. Our millimeter-sized bubbles are so spherical that the tiny gravity-induced pressure difference between their top and bottom becomes the dominant source of jet formation. To our knowledge, this experiment provides the first clean movies of gravity-jets in normal gravity conditions. Similar observations in the past [7] required large bubbles ($R_0 > 1$ cm) in hyper-gravity.

The four controllable experimental parameters are the maximal bubble radius R_0 (varied in the range $1-7$ mm), the liquid pressure at cavity level p_0 ($8 - 80$ kPa), the norm of the pressure gradient $|\nabla p|$ ($0 - 18\,\mathrm{kPa\,m^{-1}}$), and the dynamic viscosity η ($1 - 30$ mPa s). These parameters are controlled as follows: A pressure-regulated vacuum pump depressurizes the liquid at a precision of 0.2 kPa, while also removing traces of laser-generated gas. The flight manoeuvres (93 ballistic trajectories, straight cruise, 24 steep turns) provide intervals of stable gravity at '0g', '1g', '1.2g', '1.4g', '1.6g', and '1.8g' (i. e. $g = 1.8 \cdot 9.81\,\mathrm{m\,s^{-2}}$), as well as transition phases,

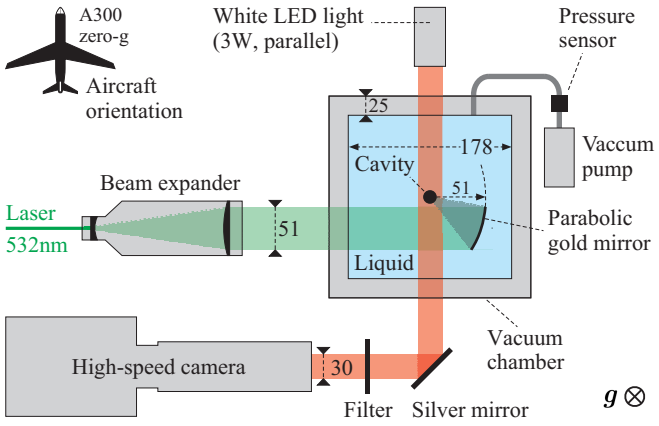

FIG. 2: Schematic view of the experiment flown on parabolic flights. The test-chamber, filled with a water-glycerine mixture of adjustable viscosity, is pressure-controlled. An ultraspherical cavitation bubble is produced by a 8 ns laser pulse focused with a parabolic mirror at a high convergence angle of 53°. (Dimensions in mm)

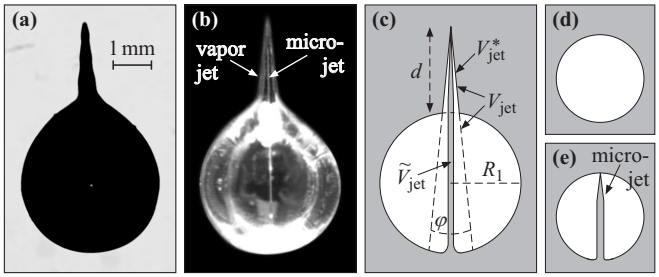

FIG. 3: (a, b) Observations of the gravity-driven jet of a rebounding cavitation bubble ($R_0 = 3$ mm, $\Delta p = 10$ kPa) in normal gravity: (a) using a back-illumination (see Fig. 2), (b) using a front-illumination and adaptive overlaying of different exposures to increase the dynamic range and sharpness. The vapor jet envelops a narrow micro-jet in agreement with simulations [14]. (c–e) Model (see text).

thus offering a wide range of gradients $|\nabla p| = \rho g$. By adjusting the energy of the laser pulse and the pressure p_0, bubbles of various radii R_0 can be obtained. R_0 is then measured at 10 μm-accuracy on the high-speed movies (e. g. Fig. 1a, left). These movies resolve the initial growth and collapse of the bubble into more than 100 frames. Demineralized water is used in the experiments at variable gravity, while ground-based follow-up experiments use water-glycerol mixtures to expand the viscosity range from $\eta = 1$ mPa s (pure water) to $\eta = 2$ mPa s (25% glycerol mass) and $\eta = 30$ mPa s (75% glycerol). The addition of glycerol mainly alters η, but it also affects p_v, ρ, and the sound speed c. These variations are accounted for in the data analysis below (Eq. 3).

Experimental results – Observations of rebounding bubbles with a gravity-jet are shown in Figs. 1a, 3a, 3b, 4. Most of these images use a parallel back-light (Fig. 2), hence the bubbles appear in absorption against a white background. This type of imaging allows a precise measurement of the bubble geometry and a visualization of shocks (Fig. 1a). An alternative front-illumination discloses the internal structure, namely the narrow micro-jet inside the vapor jet (Fig. 3b). The missing jet in '0g' (Fig. 1a, top) proves the gravitational origin of the jets. Rayleigh-Taylor instabilities during the rebound [19] can be excluded as jet-drivers because of the torus-topology (Fig. 3b, c).

Nearby boundaries can also cause jets by altering the pressure gradient [5, 6, 11], and they dominate over gravity if $\lambda \equiv h^2\rho g/(R_0\Delta p) < 0.2$ [square of Eq. 8.8 in Ref. 16]. Here, $h = 55$ mm is the distance from the parabolic mirror to the bubble centre. To guarantee accurate results we only retain gravity-dominated cases with $\lambda \geq 0.5$, thus keeping a sample of 104 bubbles with jets. Yet, many small bubbles ($R_0 \lesssim 2.5$ mm, thus $h/R_0 \gtrsim 22$) in '0g' ($\lambda = 0$) yield no jet (Fig. 1a, top), since the influence of boundaries is too weak. Albeit excluded from the analysis, these data is shown in Fig. 4 as a single point.

For each bubble in the sample, each high-speed image of the rebound phase is decomposed into a circu-

lar disk and a jet, using a χ^2-fit of a circular top-hat function. The jet volume $V^*_{\rm jet}$ (vapor+liquid, Fig. 3c) is then calculated assuming axial symmetry about the jet-axis. Since $V^*_{\rm jet}$ only contains a part of the micro-jet, we define an effective volume $V_{\rm jet}$ as the geometrical extension of $V^*_{\rm jet}$ into the bubble (Fig. 3c) – an approach justified in § 'theoretical model'. The relation between $V_{\rm jet}$ and $V^*_{\rm jet}$ depends on the cone angle φ. This angle is measured along the edges of the vapor jet rather than at its tip to bypass potential deformations of the tip by surface tension. When $V^*_{\rm jet}$ is maximal, we observe $\varphi \approx 4°$ across all bubbles. Trigonometry then implies [26] $V^{\rm max}_{\rm jet} = (V^{*\,\rm max 1/3}_{\rm jet} + 0.2R_1)^3$ where R_1 is the maximal bubble radius during the rebound. We finally define a "normalized jet volume" as

$$\epsilon_{\rm jet} \equiv V^{\rm max}_{\rm jet}/[(4\pi/3)R_1^3]\,. \qquad (2)$$

Aiming for a model of $\epsilon_{\rm jet}$, we adopt the Ansatz that $\epsilon_{\rm jet}$ is proportional to a non-dimensional parameter ζ, defined as a power law of the parameters R_0, ρ, g, p_0, η, and the liquid compressibility (sound speed c). The surface tension σ is neglected as justified for our relatively large bubbles [27], but we will show (theory below) that even the jets of much smaller bubbles remain insignificantly affected by surface tension. The most general non-dimensional form of ζ then reads

$$\zeta = \left(R_0^\alpha\, \rho^\beta\, g\, \Delta p^{\alpha-\beta-1}\, c^{-\alpha+2\beta-1}\, \eta^{-\alpha+1}\right)^\gamma\,, \qquad (3)$$

where α, β, γ are free parameters. To determine α, β, γ we perform a χ^2-fit, minimizing the uncertainty-weighted rms of $\epsilon_{\rm jet}/\zeta$ over the 104 data points. This yields $\alpha = 1.04 \pm 0.03$, $\beta = 1.05 \pm 0.20$, $\gamma = 0.98 \pm 0.10$ (with $\chi^2 = 0.9$), where the ranges are 67% confidence intervals obtained by bootstrapping the data [20]. Since $\alpha = \beta = \gamma = 1$ is consistent with the data, it seems natural to adopt this choice. Substituting $|\boldsymbol{\nabla} p| = \rho g$ then reduces Eq. (3) to

$$\zeta = |\boldsymbol{\nabla} p|\, R_0/\Delta p\,. \qquad (4)$$

Fig. 4 shows the measured values of $\epsilon_{\rm jet}$ as a function of ζ together with the linear regression (solid line)

$$\epsilon_{\rm jet} = 5.4\,\zeta\,. \qquad (5)$$

A remarkable feature of this proportionality relation (Eqs. 4, 5) is its independence of the viscosity η, as verified for η-variations by a factor 30 (Fig. 4).

If no vapor jet is observed ($V^{*\,\rm max}_{\rm jet} = 0$), Eq. (2) implies $\epsilon_{\rm jet} = \epsilon^{\rm min}_{\rm jet} \approx 0.002$. The inequality $\epsilon^{\rm min}_{\rm jet} > 0$ reflects that when no vapor jet forms, a micro-jet may still be present. In fact, no vapor jet arises in all cases between no micro-jet (Fig. 3d) and a micro-jet that just touches the bubble surface (Fig. 3e). This range of indeterminacy is shaded in Fig. 4. Using Eq. (5) the threshold value $\zeta_{\rm c}$, where $\epsilon_{\rm jet}(\zeta_{\rm c}) = \epsilon^{\rm min}_{\rm jet}$, reads $\zeta_{\rm c} \approx 4 \cdot 10^{-4}$. The jet only pierces the bubble surface if $\zeta > \zeta_{\rm c}$, i. e. $\zeta_{\rm c}$ delimits the topological transition between a sphere and a torus.

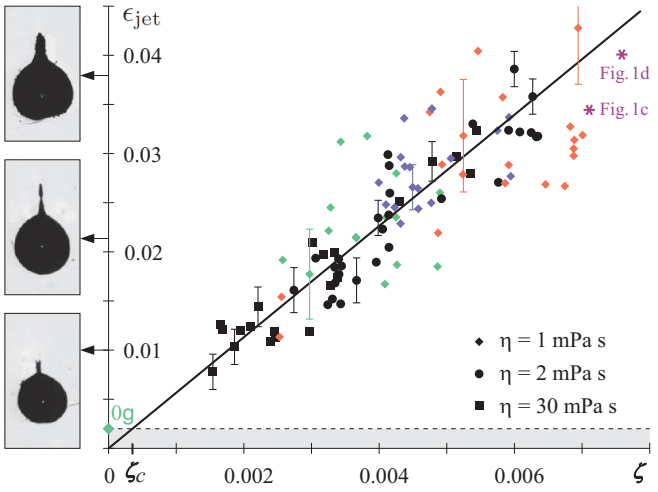

FIG. 4: Scaling law. Black points are data at varying R_0, p_0, η and fixed $g = 9.81\,\mathrm{m\,s^{-2}}$. Colored points are data at varying R_0, p_0, g and fixed $\eta = 1\,\mathrm{mPa\,s}$ (green: $g < 11\,\mathrm{m\,s^{-2}}$, red: $g > 16\,\mathrm{m\,s^{-2}}$, blue: intermediate). Some 67% measurement uncertainties are shown by the error bars. The solid line is the weighted regression (Eq. 5). The zone of experimental indeterminacy, covering the cases between Fig. 3d and Fig. 3e, is grey-shaded.

To confirm this conjecture further investigations of this transition are needed.

Theoretical model – The relation $\epsilon_{\rm jet} \propto \zeta$ will now be derived from first principles. By conservation of momentum, the micro-jet momentum equals the integrated momentum accumulated by the liquid during the bubble growth and collapse. This momentum, called "Kelvin impulse", was explored by Blake [16]. It can be computed as $\boldsymbol{I} = \int_{-T_{\rm c}}^{T_{\rm c}} \mathrm{d}t \int_{S(t)} \mathrm{d}\boldsymbol{F}$, where $T_{\rm c}$ is the collapse time, S is the bubble surface (here assumed spherical), and $\mathrm{d}\boldsymbol{F} = -p\,\mathrm{d}\boldsymbol{S}$ is the force acting on the bubble surface. Spherically symmetric (isotropic) terms in the pressure field p vanish in the integral over S. Hence, we only consider anisotropic pressure terms, here given by a constant $\boldsymbol{\nabla} p$, defined as the pressure gradient in the absence of a bubble. The bubble adds an additional gradient that varies with the normalized time $\tau \equiv t/T_{\rm c}$. This bubble-generated gradient contains a radial, spherically symmetric term (§3.2.3 in [21]) vanishing in the momentum integral, and a linear term proportional to $\boldsymbol{\nabla} p$ caused by the motion of the bubble center. Thus, neglecting isotropic terms, $\mathrm{d}\boldsymbol{F} = -f(\tau)(\boldsymbol{\nabla} p \cdot \boldsymbol{R})\,\mathrm{d}\boldsymbol{S}$, where $f(\tau)$ is a scalar function and $\boldsymbol{R}(t)$ is the vector from the bubble center to a surface element. In this generic model, the micro-jet momentum $\boldsymbol{I}$ solves to [28]

$$\boldsymbol{I} \propto -\boldsymbol{\nabla} p R_0^3 T_{\rm c}\,. \qquad (6)$$

$T_{\rm c}$ is the key term, where side-effects can intervene. While the Rayleigh-theory [22] implies $T_{\rm c} \approx 0.915 R_0\sqrt{\rho/\Delta p}$, the Plesset-theory [23] details that: (i) Incondensable gas increases $T_{\rm c}$ (see § 'Discussion'). (ii)

Surface tension decreases T_c – by less than 1% for our bubbles and by about 7% for a micro-bubble ($R_0 = 10\,\mu$m) in water at standard conditions ($\sigma = 0.07\,\mathrm{N\,m^{-1}}$, $p_0 = 10^5\,\mathrm{Pa}$). Carried along to Eq. (8b), this 7%-effect reduces the jet mass by only 14%, comparable to a $1\,\mu$m-measurement error of R_0. (iii) Viscosity increases T_c for small bubbles, but the effect is even weaker – about 1% for a bubble with $R_0 = 10\,\mu$m (at $\eta = 1\,\mathrm{mPa\,s}$, $p_0 = 10^5\,\mathrm{Pa}$). Hereafter T_c in Eq. (6) will hence be approximated as $0.915 R_0\sqrt{\rho/\Delta p}$.

In analogy to the "Kelvin impulse" we now introduce a kinetic "Kelvin energy" $E = 2\int_0^{R_0}\int_{S(t)} |\mathrm{d}\boldsymbol{F}\cdot\mathrm{d}\boldsymbol{R}|$, resulting from the work done by the same anisotropic forces that generate the jet's momentum. Thus [29],

$$E \propto |\boldsymbol{\nabla} p|\, R_0^4\,. \tag{7}$$

Defining m and $\boldsymbol{v}$ as the mass and spatially averaged velocity of the fully developed micro-jet (Fig. 3) implies $\boldsymbol{I} = m\boldsymbol{v}$ and $E \propto m\boldsymbol{v}^2$. Eqs. (6, 7) then yield

$$\boldsymbol{v} \propto -\sqrt{\Delta p/\rho}\;\hat{\mathbf{e}}\,, \tag{8a}$$

$$m \propto |\boldsymbol{\nabla} p|\, R_0^4\, \rho/\Delta p\,, \tag{8b}$$

where $\hat{\mathbf{e}} \equiv \boldsymbol{\nabla} p/|\boldsymbol{\nabla} p|$. Eq. (8a) is a known relation [8], while Eq. (8b) is of interest regarding the jet volume. We hypothesize that the effective jet volume scales with the micro-jet volume, $V_{\mathrm{jet}}^{\max} = \varepsilon\, m\, \rho^{-1}$, at an efficiency $\varepsilon \propto R_1^3/R_0^3$. This approximation derives from the observation that the vapor jet grows out of the rebound bubble, thus consuming a fraction of the rebound volume $\propto R_1^3$. Eqs. (2, 8b) then imply

$$\epsilon_{\mathrm{jet}} \propto |\boldsymbol{\nabla} p|\, R_0/\Delta p \equiv \zeta\,. \tag{9}$$

Alternatively, Eq. (9) also results from assuming ϵ_{jet} proportional to E/E_0, where $E_0 = (4\pi/3)R_0^3\Delta p$.

Discussion – In summary, Eqs. (5, 9) demonstrate experimentally and theoretically that the normalized jet volume ϵ_{jet} is proportional to ζ. Along this discovery subtle issues were encountered that are worth explaining: (i) Eq. (9) is not 'scale invariant' as it depends on R_0: given $\boldsymbol{\nabla} p$, big bubbles yield larger ϵ_{jet} than small ones. Formal scale invariance is nonetheless recovered using an adequately normalized gradient $\tilde{\boldsymbol{\nabla}} \equiv \sum_{\mathrm{i}=1}^{3} \partial/(\partial x_{\mathrm{i}}/R_0)\hat{\mathbf{e}}_{\mathrm{i}}$ $\Rightarrow \zeta = |\tilde{\boldsymbol{\nabla}} p|/\Delta p$. (ii) How can a micro-jet survive inside the hot gas [24] during the collapse point? This feature might be attributed to the life-time of the hot gas ($< 1\,\mu$s, [24]) being too short to evaporate the jet. (iii) We neglected incondensable gas inside the bubble, since the measured bubble radii $R(t)$ agree within 1% with the Rayleigh-equation [22], when neglecting incondensable gas. If bubbles contain significant amounts of incondensable gas, they do not fully collapse, hence less concentrating their Kelvin-impulse. (iv) While Eqs. (5, 9) rely on stationary $\boldsymbol{\nabla} p$'s, they also approximate non-stationary situations, if the characteristic time-scales are comparable to or above T_c. This is illustrated by the data of Figs. 1c, d (where $\epsilon_{\mathrm{jet}} = 0.2\, R_0^2\, h^{-2}$) plotted as stars in Fig. 4. (v) We here considered jet parameters $\zeta < 0.008$. Larger ζ may produce more complex bubble-jet morphologies, requiring a decomposition into spherical harmonics.

Supported by the European Space Agency ESA and the Swiss NSF (200020-116641, PBELP2-130895).

[1] T. J. Mason, L. Paniwnyk, and J. P. Lorimer, Ultrasonics Sonochemistry **3**, 253 (1996).
[2] R. Dijkink and C.-D. Ohl, Lab on a Chip **8**, 1676 (2008).
[3] T. G. Leighton and R. O. Cleveland, Proc. Inst. Mech. Eng. H **224**, 317 (2010).
[4] J. P. Dear and J. E. Field, J. Fluid Mech. **190**, 409 (1988).
[5] A. Philipp and W. Lauterborn, J. Fluid Mech. **361**, 75 (1998).
[6] C.-D. Ohl, M. Arora, R. Dijkink, V. Janve, and D. Lohse, Applied Physics Letters **89**, 074102 (2006).
[7] T. B. Benjamin and A. T. Ellis, Phil. Trans. R. Soc. Lond. A **260**, 221 (1966).
[8] M. Plesset and R. B. Chapman, J. Fluid Mech. **47**, 283 (1971).
[9] J. I. Katz, Proc. R. Soc. Lond. A **455**, 323 (1999).
[10] J. P. Dear, J. E. Field, and A. J. Walton, Nature **332**, 505 (1988).
[11] G. L. Chahine, Appl. Sci. Res. **38**, 187 (1982).
[12] D. Obreschkow, P. Kobel, N. Dorsaz, A. de Bosset, C. Nicollier, and M. Farhat, Phys. Rev. Lett. **97**, 094502 (2006).
[13] P. Kobel, D. Obreschkow, N. Dorsaz, A. De Bosset, and M. Farhat, Experiments in Fluids **47**, 39 (2009).
[14] J. R. Blake, G. S. Keen, R. P. Tong, and M. Wilson, Philos T R Soc A **357**, 251 (1999).
[15] F. Avellan, P. Henry, and I. Rhyming, Proc. Int. Symp. on Cav. Research Facilities and Tech. **57**, 49 (1987).
[16] J. R. Blake, J. Austr. Math. Soc. B **30**, 127 (1988).
[17] K.-T. Byun and H.-Y. Kwak, Japanese Journal of Applied Physics **43**, 621 (2004).
[18] W. Lauterborn, Applied Physics Letters **21**, 27 (1972).
[19] D. Frost and B. Sturtevant, J. Heat Transfer-Trans. ASME **108**, 418 (1986).
[20] B. Efron, J. Am. Stat. Assoc. **82**, 171 (1987).
[21] J.-P. Franc and J.-M. Michel, *Fundamentals of Cavitation* (Kluwer Academic Publishers, 2004).
[22] L. Rayleigh, Phil. Mag. **34**, 94 (1917).
[23] M. S. Plesset and A. Prosperetti, Annual Review of Fluid Mechanics **9**, 145 (1977).
[24] O. Baghdassarian, H.-C. Chu, B. Tabbert, and G. A. Williams, Phys. Rev. Lett. **86**, 4934 (2001).
[25] 53rd ESA Parabolic Flight Campaign, October 2010
[26] Define $z^3 \equiv (\pi/3)\tan^2(\varphi/2) \Rightarrow V_{\mathrm{jet}}^* = z^3 d^3$ and $V_{\mathrm{jet}} =$

$z^3(d+2R_1)^3 = (zd+2zR_1)^3 \approx (V_{\rm jet}^{*1/3}+0.2R_1)^3$.

[27] The "Rayleigh pressure" $\Delta p + \frac{3}{2}\rho\dot{R}^2(t)$ exceeds the "surface pressure" $2\sigma/R(t)$ by a factor $> 10^2$ at all times $t \in [0, T_{\rm c}]$ for bubbles of $R_0 > 0.1\,$mm at $p_0 = 1\,$bar and $R_0 > 1\,$mm at $p_0 = 0.1\,$bar. Strictly, this argument is restricted to a spherical collapse; see § 'theoretical model' for an extension to jets.

[28] Use spherical coord. (R, ϕ, θ) with $\theta \equiv \angle(\boldsymbol{\nabla} p, \boldsymbol{R}) \Rightarrow \boldsymbol{\nabla} p \cdot \boldsymbol{R} = |\boldsymbol{\nabla} p| R\cos\theta$. Only the z-projection of $\mathrm{d}\boldsymbol{S}$, $\mathrm{d}S_{\rm z} = \mathrm{d}\phi\,\mathrm{d}\theta R^2 \sin\theta\cos\theta$, persists in the ϕ-integral $\Rightarrow \int_{S(t)} \mathrm{d}\boldsymbol{F} = -fR^3\boldsymbol{\nabla} p \int_0^{2\pi}\mathrm{d}\phi \int_0^{\pi} \sin\theta\,\cos^2\theta\,\mathrm{d}\theta \Rightarrow \boldsymbol{I} = -(4\pi/3)\boldsymbol{\nabla} p \int_{-T_{\rm c}}^{T_{\rm c}} fR^3\mathrm{d}t$. According to Rayleigh $R(t) = R_0\tilde{R}(\tau)$, where $\tilde{R}(\tau)$ is a unique function, as is $f = f(\tau)$ $\Rightarrow \boldsymbol{I} = -(4\pi/3)\boldsymbol{\nabla} p R_0^3 T_{\rm c} \int_{-1}^{1} f(\tau)\tilde{R}(\tau)^3\mathrm{d}t \propto -\boldsymbol{\nabla} p R_0^3 T_{\rm c}$.

[29] Use spherical coord. as above. Thus, $\mathrm{d}\boldsymbol{F}\cdot\mathrm{d}\boldsymbol{R} = \mathrm{d}R\,\mathrm{d}\phi\,\mathrm{d}\theta\,|\boldsymbol{\nabla} p| fR^3\sin\theta\cos\theta \Rightarrow \int_{S(t)} |\mathrm{d}\boldsymbol{F}\cdot\mathrm{d}\boldsymbol{R}| = 2\pi|\boldsymbol{\nabla} p| fR^3\mathrm{d}R$. Since f can be rewritten as a function of R/R_0, $\int_0^{R_0} fR^3\mathrm{d}R \propto R_0^4 \Rightarrow$ Eq. (7).